Nanotechnology Perceptions
ISSN 1660-6795
www.nano-ntp.com

Modelling a Grid-Connected Variable Speed Wind Energy Conversion System Using SCIG With a Study of the Factors Affecting its Output Power

Mohamed M Rabiee[1], Ahmed M. Othman[2], Mahdi M El-Arini[2]

[1]*Electrical Power and Machines Department, Faculty of Engineering, Zagazig University, Egypt.*
[2]*Professor, Electrical Power and Machines Department, Faculty of Engineering, Zagazig University, Egypt.*
Email: m.rabia021@eng.zu.edu.eg

This paper examines the modelling, simulation, and optimisation of wind turbine electrical systems within the operational and theoretical frameworks of hybrid microgrids. It engages with the mechanisms of wind energy conversion and the relationship between its generation processes and the structural and functional dynamics of the Wind Energy Conversion System (WECS). The detailed analysis presented explores WECS's core components such as aerodynamic control subsystems, drivetrain configurations, and generator operations, which collectively influence energy conversion efficiency. Using advanced simulations in MATLAB/Simulink, the study evaluates the impact of critical parameters such as wind speed, pitch angle, and rotor blade dimensions, and provides a methodologically robust investigation into their roles in maximising power output. This research further contributes to the understanding of how precise design and operational control strategies support the integration of wind energy within hybrid systems, and aims to offer perspectives on the interdependent factors necessary for advancing resilient and sustainable renewable energy solutions.

Keywords: Wind Energy, Wind Energy Conversion System (WECS), Wind Turbine (WT), Squirrel Cage Induction Generator (SCIG), Drive Train, Tip Speed Ratio (TSR), and Simulink

1. Introduction

The escalating global demand for energy and the pressing environmental consequences of

fossil fuel consumption have catalysed a worldwide shift toward renewable energy solutions. Within this transition, wind energy has emerged as an alternative that offers a source of power which is inherently clean, sustainable, and abundant in nature. Central to harnessing this resource are wind turbines, which convert the kinetic energy of wind into electrical power, making such alternative indispensable to modern energy systems. Yet, despite their potential, optimising the performance of wind turbines presents a challenge within the context of hybrid microgrids where diverse energy sources must operate in harmony to maintain system stability and operational efficiency [1].

This paper examines the modelling and performance enhancement of wind turbine electrical systems within hybrid microgrids by employing advanced simulation techniques to investigate operational parameters. By addressing the technical complexities of wind energy systems, the study demonstrates the potential of these technologies to reduce emissions, lower operational costs, and improve the reliability of energy supply [2]. Egypt, endowed with substantial wind resources, is explored as a practical case study, with the Gulf of Suez identified as a region of particular significance due to its high wind speeds and capacity for large-scale wind energy deployment [3]. These conditions position the Gulf of Suez as a focal point for renewable energy initiatives and a model for integrating wind energy into national energy strategies.

The study extends beyond the environmental and economic advantages of wind energy, engaging with its technical dimensions, including the optimisation of aerodynamic controls and other critical subsystems. Through a comprehensive analysis of these factors, the research contributes to the broader effort to integrate wind energy into sustainable energy frameworks, advancing the global pursuit of energy systems less [4] dependent on fossil fuels.

2. Wind Energy in Egypt

Egypt possesses substantial renewable energy resources, with wind energy emerging as a key contributor to the nation's energy transition strategy. The Gulf of Sue is recognised for its high wind speeds ranging from 9 to 12 m/s, making it one of the most promising regions for wind power development. As identified in the Wind Atlas of Egypt in Figure 1, this region offers the potential to support large-scale wind farms capable of generating considerable clean energy to meet the growing electricity demands of a rapidly expanding population [5].

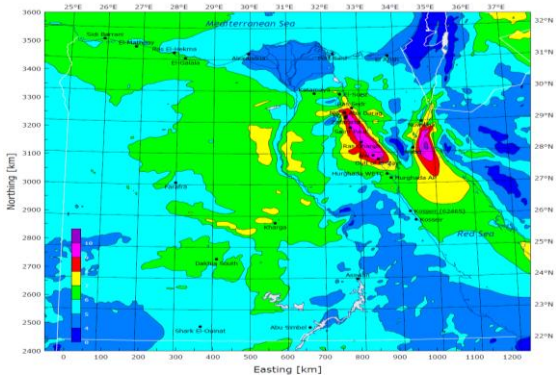

Figure 1: Wind Atlas of Egypt

Significant governmental investments have been directed towards wind power projects, exemplified by key developments such as the Zafarana Wind Farm and the Jabal Al-Zayt Wind Farm. The Zafarana Wind Farm, one of the earliest large-scale projects in the region, has achieved a generation capacity exceeding 500 MW, while the Jabal Al-Zayt Wind Farm, incorporating advanced technological innovations, has further bolstered contributions to the national grid [6]. These projects align with Egypt's renewable energy targets, which aim to derive 42% of the country's electricity from renewable sources by 2035 and mark a decisive shift away from reliance on fossil fuels.

The development and exploitation of renewable energy sources are expected to help establish new cities and stimulate investments, which would, in turn, contribute to economic growth and the creation of employment opportunities. New and Renewable Energy Authority NREA [7] was established in 1986 to represent the use and development of renewable energy technology in Egypt and its commercial use.

The adoption of wind energy in Egypt is driven by several factors: favourable geographic conditions, increasing energy demands, and the need to reduce greenhouse gas emissions. Nonetheless, the sector faces challenges concerning grid integration, operational efficiency, and maintenance in the harsh conditions of desert environments. Advanced modelling and optimisation techniques, as discussed in this paper, offer viable solutions to these challenges, enabling the effective expansion and integration of wind energy across the national grid.

As a result of relying on clean energy, the amount of fuel used in energy production has been reduced, as well as the number of emissions resulting from the use of fossil fuels. Figure 2 shows the reduction in emissions (thousand tons of Carbon Dioxide) and the Fuel savings in thousand BP.

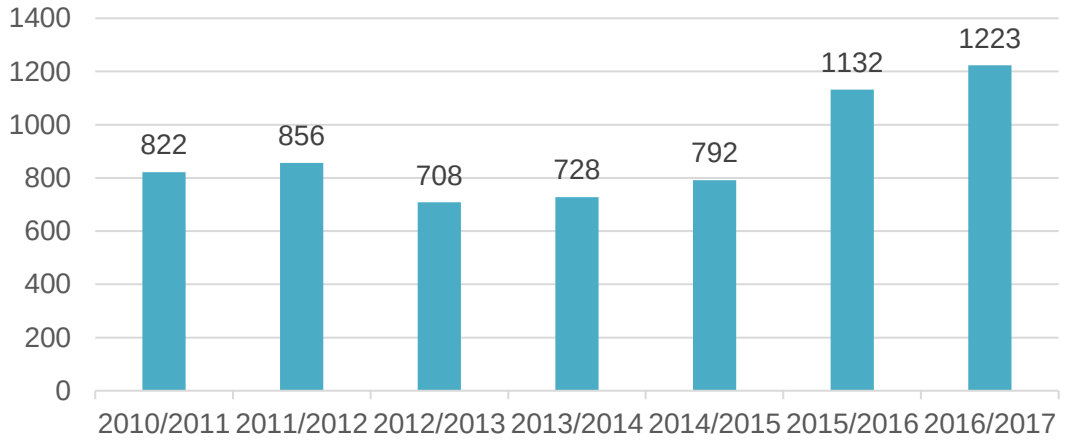

(a) Reduction in emission (thousand tons of Carbon Dioxide)

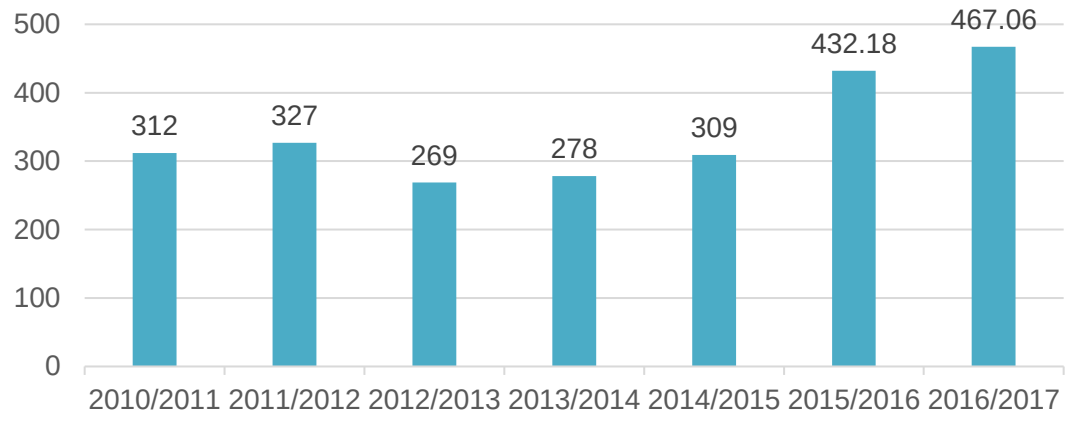

(b) Fuel savings (Thousand BP)

Figure 2: Statistics on the use of renewable energy as an alternative to fossil fuels

3. Wind Energy Conversion System (WECS)

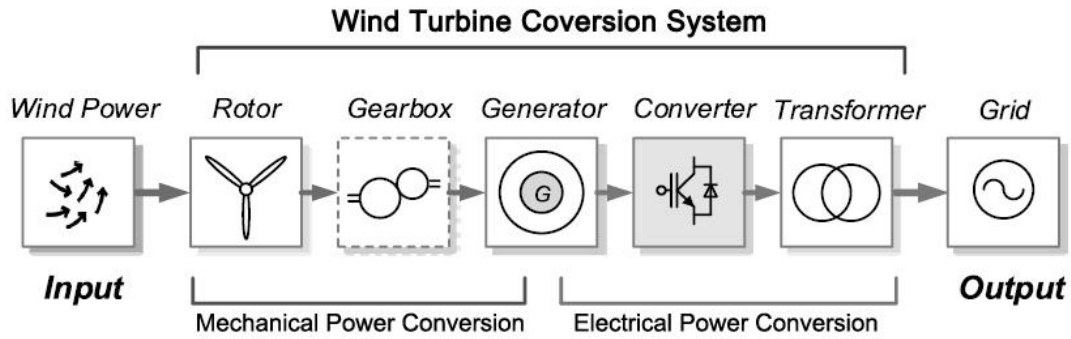

Figure 3: schematic diagram of Wind Energy Conversion System

Wind Energy Conversion System (WECS) is the process of generating electricity from wind. It consists of two stages; the first stage is to convert the kinetic energy of the wind to mechanical energy using the rotor hub of the turbine and then perform speed multiplication using the gearbox. The second stage is transforming the mechanical power of the rotating shaft into electric power using a generator as shown in Figure 3. In the case of using the wind turbine to support small loads, the generator is directly connected to the loads. When the wind turbine is connected to the grid, a transformer is used to step the voltage up to match the grid voltage. The input of the WESC is wind energy so, it is considered a main factor to determine the electric output power of the wind turbine [8].

4. Wind Energy Characteristics

4.1- Mechanical Power extracted from the Wind

The following equation gives the power extracted from the wind.

$$\mathrm{P_{wind}} = \frac{1}{2}\rho \mathrm{A V_{wind}^3} \quad (1)$$

The mechanical output power of the turbine is a percentage of the wind power determined according to the value of the performance coefficient of this turbine.

$$\mathrm{P_{mech}} = \mathrm{C_p}(\lambda, \beta)\mathrm{P_{wind}} = \frac{\rho \mathrm{A}}{2}\mathrm{C_p}(\lambda, \beta)\mathrm{V_{wind}^3} \quad (2)$$

where,

$\mathrm{P_{wind}}$	Power extracted from the wind (W)
$\mathrm{P_{mech}}$	Mechanical output power of the turbine
V_{wind}	Wind speed (m/s)
A	Turbine swept area (m^2)
ρ	Air density (kg/m^3)
C_p	Performance coefficient of the turbine
λ	Tip speed ratio
β	Pitch angle (deg)

4.2- Tip Speed Ratio (TSR)

The tip speed ratio of the turbine, λ, or TSR, is the ratio between the linear speed of the blades and the wind speed [9]. TSR is related to the turbine's efficiency with the optimum design of the blades. The tip speed ratio of the blade can be calculated from eq (3):

$$\lambda = \frac{\omega R}{V_{wind}} \quad (3)$$

Where R is the rotor radius (m). and ω is the rotational speed of the rotor (rad/s).

4.3- Performance Coefficient (C_p)

Performance coefficient of the turbine C_p is a coefficient that depends on the pitch angle (β) of the wind turbine blade, and the tip speed ratio (λ). It is the ratio of the captured mechanical power by the turbine to the available wind energy[10]. C_p varies from turbine to another one and can be given by the following expression:

$$C_p(\lambda, \beta) = c_1\left(\frac{c_2}{\lambda_i} - c_3\beta - c_4\right)e^{\left(\frac{c_5}{\lambda_i}\right)} + c_6\lambda \quad (4)$$

$$\frac{1}{\lambda_i} = \frac{1}{(\lambda + 0.08\beta)} - \frac{0.035}{(\beta^3 + 1)} \quad (5)$$

And the constants are $c_1 = 0.5$, $c_2 = 116$, $c_3 = 0.4$, $c_4 = 5$, $c_5 = 21$ and $c_6 = 0.0068$.

According to Betz's law, there is no turbine can convert all wind energy to mechanical power but can only convert less than 59.3% of the kinetic wind energy[11]. This constant is known as Betz's coefficient. The real performance coefficient of the turbine C_p is much lower than its theoretical limit, usually ranging from 20 to 50% from power extracted from the wind.

4.4- Mechanical Torque from Wind Turbine

The mechanical torque extracted from the wind turbine[12] in $(N.m)$ can be calculated from

$$T = \frac{P_m}{\omega} \quad (6)$$

4.5- Wind Speed

Wind speed is considered the main factor that determines the electrical output power of the wind turbine system. Eq (2) shows that the output power of the turbine is directly proportional to the cube of wind speed[13]. Wind turbines can only work in a predetermined range of wind speeds. The cut-in and cut-out speeds define the range's boundaries. Wind turbine parameters are illustrated in Table 1, where the cut-in and cut-out speeds are linked to the turbine design and are decided on before construction.

Table 1: (5 KW) wind turbine parameters

Symbol	Parameter	Value
$\boldsymbol{\rho}$	Air density	$\mathbf{1.225\ kg/m^3}$
$\boldsymbol{V_{windci}}$	Cut-in wind speed	$\mathbf{3\ m/sec}$
$\boldsymbol{V_{windco}}$	Cut-out wind speed	$\mathbf{23\ m/sec}$
$\boldsymbol{D_{tg}}$	Friction in flexible coupling	$\mathbf{0.02\ Nms/rad}$
$\boldsymbol{D_t}$	Friction in wind turbine shaft	$\mathbf{0.002\ Nms/rad}$
$\boldsymbol{D_g}$	Friction of generator	$\mathbf{0.002\ Nms/rad}$
$\boldsymbol{J_g}$	Inertia constant of the generator	$\mathbf{0.001\ kg.m^2}$
$\boldsymbol{J_t}$	Inertia constant of the turbine	$\mathbf{0.1\ kg.m^2}$
$\boldsymbol{C_p}$	Power coefficient	$\mathbf{0.45}$
$\boldsymbol{P}$	Rated power	$\mathbf{5\ kW}$
$\boldsymbol{V_{wind}}$	Rated wind speed	$\mathbf{12\ m/sec}$
$\boldsymbol{R}$	Rotor radius	$\mathbf{1.91\ m}$
$\boldsymbol{K_{ss}}$	Stiffness in flexible coupling	$\mathbf{20\ Nm/rad}$

The cut-in speed refers to the wind speed at which the turbine's rotor begins to rotate, initiating the generation of electrical output power. As the wind speed increases and reaches its rated value, the turbine generates its rated power and continues to do so until the wind speed

approaches the cut-out speed. Once the wind speed surpasses the cut-out speed, the turbine must be halted to safeguard its machinery, at which point no power is generated [14].

5. Wind Turbine Model

From eq (2) the mechanical output power of the turbine is governed by five input parameters: the blade length of the turbine, which determines the turbine's swept area; wind speed; air density; angular speed of the rotor; and pitch angle. The equations outlined earlier can be implemented in MATLAB Simulink blocks to model the wind turbine, as shown in Figure 4.

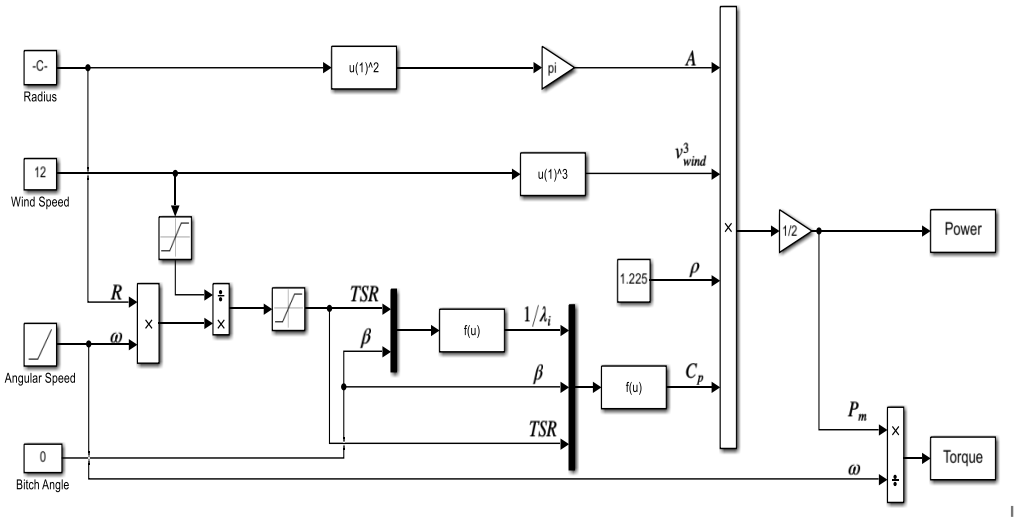

Figure 4: Wind turbine model in MATLAB Simulink

Another method to simulate the wind turbine using a MATLAB Function block is shown in Figure 5.

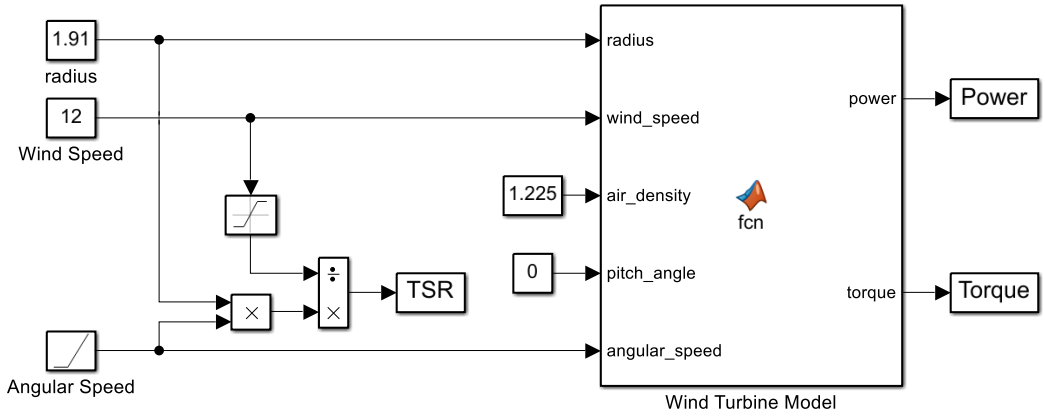

Figure 5: Wind turbine model using a MATLAB Function block.

Figure 6 shows the MATLAB function of the wind turbine in editor block:

```
function [power,torque] = fcn(radius,wind_speed,air_density,pitch_angle,angular_speed)
a=pi*radius*radius;
lambda=angular_speed*radius/wind_speed;
lambda_i=(1/(lambda+0.08*pitch_angle))-(0.035/((pitch_angle^3)+1));
c_p=0.5*(116*lambda_i-0.4*pitch_angle-5)*exp(-21*lambda_i)+0.0068*lambda;
power = 0.5*a*air_density*(wind_speed^3)*c_p;
torque=power/angular_speed;
```

Figure 6: Wind turbine MATLAB function in editor-block

6. Factors Affecting Wind Turbine Performance

6.1- The effect of the angular speed of the rotor on the output power

The effect of the angular speed of the rotor hub on the output power of the turbine can be studied by simulating the model shown in Figure 5 in MATLAB Simulink. This simulation is performed under constant values for the radius, wind speed, air density, and pitch angle, while varying the angular speed of the rotor hub. As shown in Figure 7, the output power increases as the angular speed of the rotor hub rises, reaching its optimum value at an angular speed of 51.14, after which the power begins to decrease. The angular speed of the rotor directly influences the tip speed ratio (TSR) of the turbine, as described in equation (3).

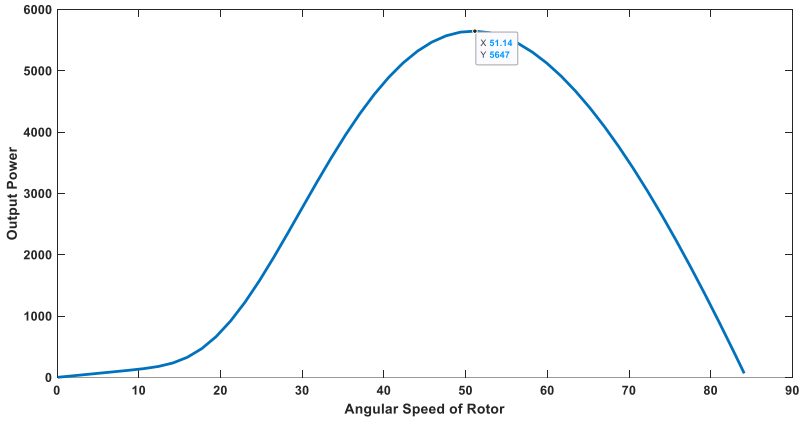

Figure 7: Effect of changing the angular speed of the rotor on the output power.

6.2- The effect of the pitch angle on the output power

Adjusting the pitch angle of the turbine blades affects the performance coefficient $\boldsymbol{C_p}$ of the turbine and consequently affects the corresponding output power. Figure 8(a) illustrates that a lower the pitch angle results in a higher C_p. Figure 8(b) further shows that at a specific TSR, the maximum C_p is achieved, and hence, the maximum output power.

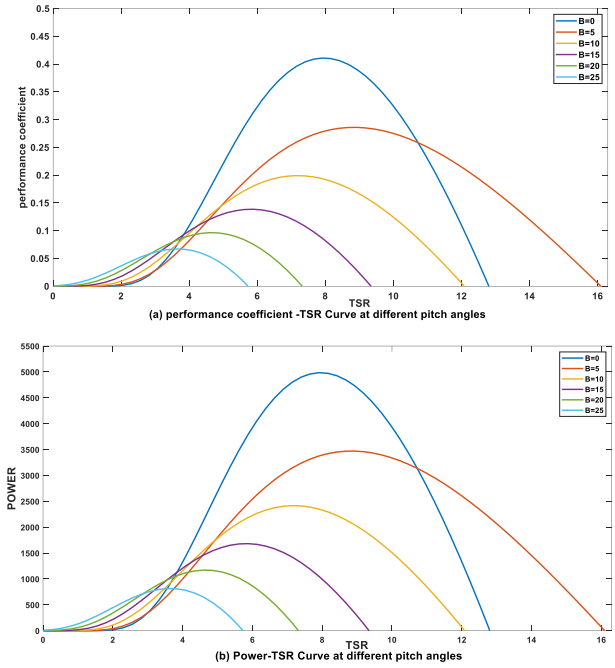

Figure 8: Effect of changing the pitch angle on the output power.

As shown in Figure 8(a), the maximum performance coefficient C_p is evidently less than the Betz limit of 0.593, which represents the theoretical maximum C_p achievable by a wind turbine.

6.3- The effect of the wind speed on the output power

As mentioned previously in the section 0, the output power of the turbine is directly proportional to the cube of wind speed. In the absence of aerodynamic wind turbine controls such as pitch control [15] or yaw control [16], the output power of the turbine at a fixed pitch angle ($\beta = 0\ deg$) is represented as shown in Figure 9.

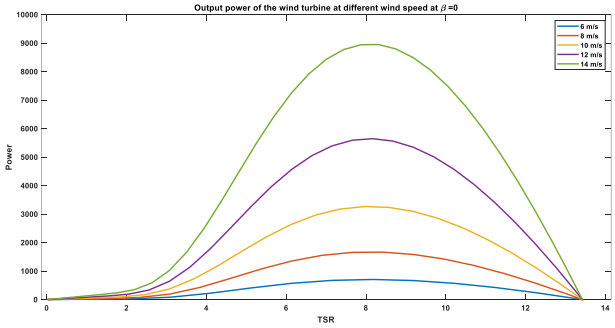

Figure 9: output power at different wind speeds at ($\beta = 0$) without any aerodynamic control.

Controlling the wind turbine is important for achieving efficient performance, minimising maintenance requirements, and optimising its operational reliability. The aerodynamic control

system improves power output, prolongs the turbine's operational lifespan, and enable safe operation by regulating the rotational speeds of both the turbine and the generator. Effective control is also necessary to maintain rated output power across a range of wind speeds and to prevent damage during high wind conditions. By adjusting the blade angle, rotational speed can be increased at low wind speeds or reduced at high wind speeds to optimise the turbine's output capacity. Pitch and yaw control are the most commonly employed methods for managing power generation, as shown in Figure 10, which illustrates their adjustment mechanisms and how they can optimise the turbine's output.

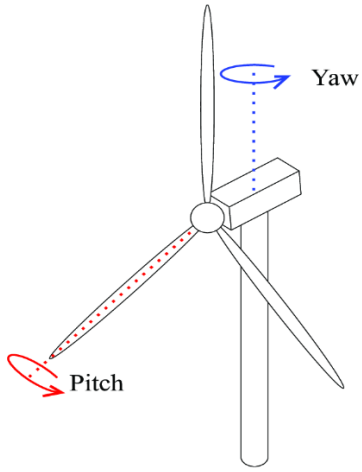

Figure 10: Pitch and yaw adjustment.

Pitch control is commonly used for large wind turbines and is performed by changing the blades' angle of attack to get the proper amount of wind to get the rated power over any wind speed within range. The blade pitch control is performed either hydraulic-controlled or electric-controlled, as shown in Figure 11. Two primary methods of pitch adjustment are generally employed: stall control and furling. Stall control is used at low wind speeds to increase energy capture by turning the blades' angle of attack into the wind, which, in turn, maximises wind energy collection and achieves rated output power. On the other hand, at high wind speeds, furling is used to turn the blades out of the wind direction, reducing rotational speed to maintain rated power or halting the turbine entirely to protect its components [17], [18].

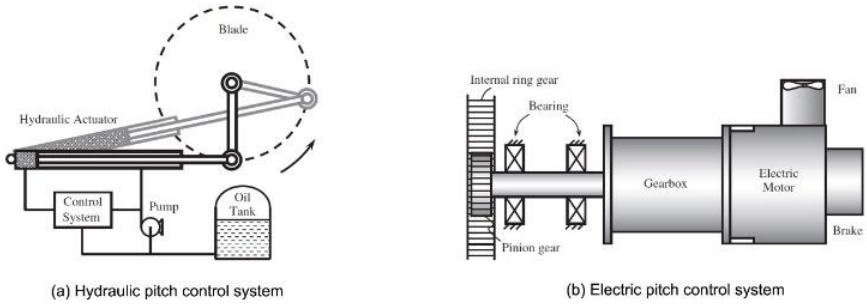

Figure 11: Types of blade pitch control systems.

When wind direction changes, the wind vane detects the new wind direction and sends it to the controller, which then drives the yaw control to rotate the entire wind turbine to face the new direction of the wind to get maximum amount of wind energy [19]. The yaw mechanism consists of multiple electric motor with a speed-reducing gearbox to rotate the entire nacelle at low rotational speed [20] as shown Figure 12. Once the nacelle aligns with the wind direction, a yaw brake is engaged to secure it in position [21].

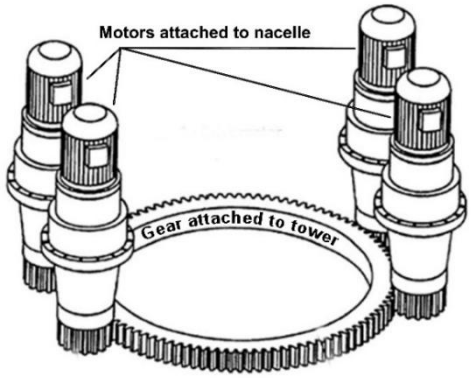

Figure 12: Yaw drive system of a large wind turbine.

Figure 13 shows the power curve of a 5 KW wind turbine as a function of wind speed, based on the aerodynamic control mechanisms previously described. In region 1, where the wind speed is below the cut-in speed, the turbine blades remain stationary, and no power is generated. In region 2, where the wind speed exceeds the cut-in speed but remains below the rated speed, the output power increases proportionally to the cube of the wind speed. In region 3, where the wind speed is greater than the rated speed but below the cut-out speed, the turbine maintains rated power generation. When the wind speed surpasses the cut-out speed, the turbine ceases operation to prevent damage, and no power is produced.

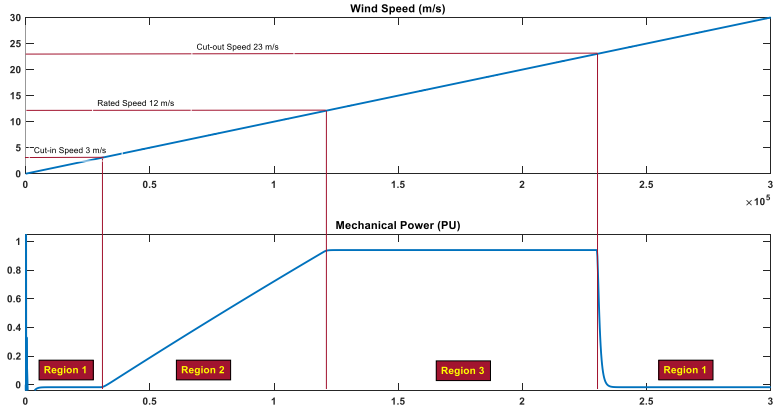

Figure 13: Power curve of wind turbine compared to wind speed.

6.4- The effect of the air density on the output power

From eq (2) the output power of a wind turbine is directly proportional to the air density. Air

density is influenced by several factors, such as height above the ground, temperature, and humidity. As the height of the turbine tower increases, air density decreases, but this is often accompanied by an increase in wind speeds. Similarly, higher temperatures and increased humidity result in lower air density. Despite the reduction in air density at higher altitudes, the corresponding increase in wind speed generally allows turbines installed at greater heights to generate more power compared to those situated at lower altitudes.

6.5- The effect of the blade length of the turbine on the output power

The blade length of a wind turbine influences two important factors: the turbine's swept area and its TSR, both of which directly affect the output power. Optimising the rotor blade length is essential during the turbine design process to achieve optimal performance, which typically involves balancing aerodynamic efficiency, structural requirements, and cost considerations. Longer blades have the capacity to capture more wind energy but necessitate stronger materials and support structures to manage increased loads. On the other hand, shorter blades may be more economical but can result in reduced energy capture efficiency. Therefore, fine-tuning the blade length is necessary to maximise efficiency and ensure reliable operation. As shown in Figure 14, the turbine begins producing mechanical power at a specific blade length, at which the output power is sufficient to overcome the generator's inertia [22].

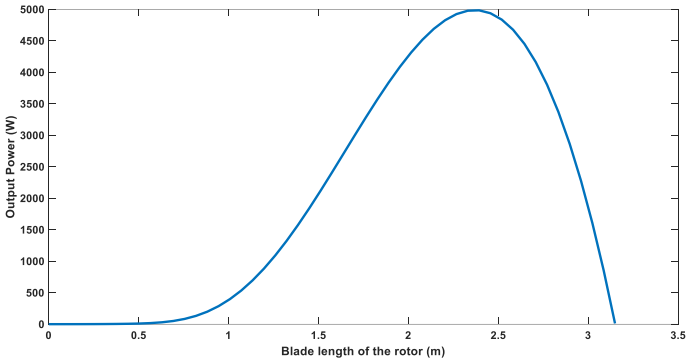

Figure 14: Effect of changing the blade length of the turbine on the output power.

Once the maximum output power is achieved at the optimum blade length, any further increase in blade length results in a reduction in power output due to the additional weight of the blades.

7. Drive Train based on a 2-Mass Model.

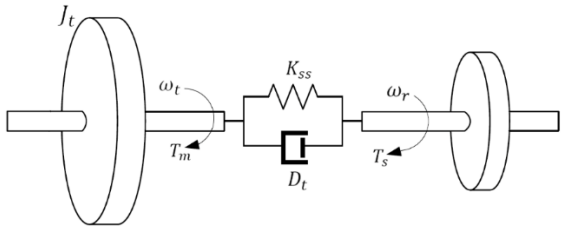

Figure 15: Two-mass spring-damper representation of the drive train.

The drive train of a wind turbine generation system connects the high-inertia turbine to the low-inertia generator through an elastic shaft, as shown in Figure 15. This configuration is commonly employed in variable-speed wind turbines and can be mathematically represented by the following three equations:

$$2J_t \frac{d\omega_t}{dt} = T_m - T_s \qquad (7)$$

$$\frac{1}{\omega_{ebs}} \frac{d\theta_{sta}}{dt} = \omega_t - \omega_r \qquad (8)$$

$$T_s = K_{ss}\theta_{sta} + D_t \frac{d\theta_{sta}}{dt} \qquad (9)$$

Where,

J_t	Inertia of the turbine
θ_{sta}	Shaft twist angle
ω_t	Angular speed of the wind turbine
ω_r	Rotor speed of the generator
ω_{ebs}	Electrical base speed
T_s	Shaft torque
T_m	Wind turbine torque
K_{ss}	Shaft stiffness
D_t	Damping coefficient

The block diagram of the drive train in MATLAB Simulink is shown Figure 16. The model has two inputs and two outputs. The inputs are the wind turbine torque and the rotor speed of the generator, where the outputs are the angular speed of the turbine and the torque of the generator shaft. The drive train parameters are illustrated in Table 1.

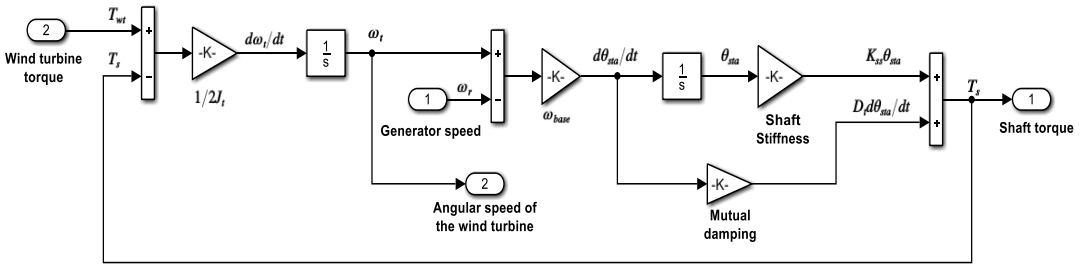

Figure 16: Wind turbine drive train based on a 2-mass model.

8. Squirrel Cage Induction Generator (SCIG)

In variable-speed wind turbines, SCIG is often the generator of choice due to its simplicity,

reliability, and suitability for achieving optimal power output when coupled with aerodynamic control methods. The SCIG's straightforward design, minimal maintenance requirements, and favourable power-to-weight ratio make it a robust option for such applications [23].

To model the induction generator, space vector theory is employed, which simplifies the analysis by representing the system with a single equivalent circuit comprising complex variables, as illustrated in Figure 17.

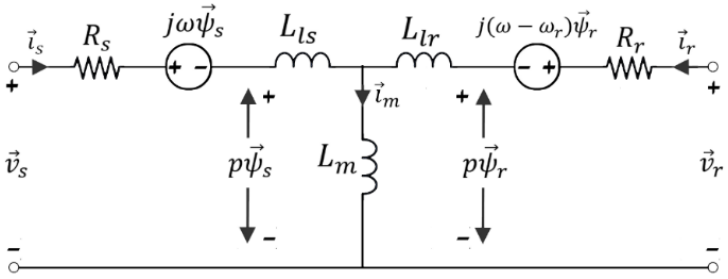

Figure 17: Space-vector equivalent circuit of the IG.

This model is defined by three sets of equations: voltage, flux linkage, and motion equations.

From Figure 17, the voltage equations are given by:

$$\begin{cases} \vec{v}_s = R_s\vec{\imath}_s + p\vec{\psi}_s + j\omega\vec{\psi}_s \\ \vec{v}_r = R_r\vec{\imath}_r + p\vec{\psi}_r + j(\omega-\omega_r)\vec{\psi}_r \end{cases} \quad (10)$$

Where,

- p derivative operator ($p = d/dt$).
- ω rotating speed of the arbitrary reference frame (rad/s)
- $\vec{\imath}_r$ rotor current vector (A)
- ω_r rotor electrical angular speed (rad/s)
- $\vec{\psi}_r$ rotor flux linkage vector (Wb)
- $\vec{v}_r$ rotor voltage vector (V)
- R_r rotor winding resistance (Ω)
- $\vec{\imath}_s$ stator current vector (A)
- $\vec{\psi}_s$ stator flux linkage vector (Wb)
- $\vec{v}_s$ stator voltage vector (V)
- R_s stator winding resistance (Ω)

The imaginary terms in eq (10) are referred to as speed voltages.

To derive the flux linkage equations of the space vector model, all the rotor-side parameters and variables are referred to the stator side. The flux linkage equation $\vec{\psi}_s$ and $\vec{\psi}_r$ are given by:

$$\begin{cases} \vec{\psi}_s = (L_{ls} + L_m)\vec{\imath}_s + L_m\vec{\imath}_r = L_s\vec{\imath}_s + L_m\vec{\imath}_r \\ \vec{\psi}_r = (L_{lr} + L_m)\vec{\imath}_r + L_m\vec{\imath}_s = L_s\vec{\imath}_s + L_m\vec{\imath}_s \end{cases} \quad (11)$$

Where,

L_s	stator self-inductance (H)
L_r	rotor self-inductance (H)
L_{ls}	stator leakage inductances (H)
L_{lr}	rotor leakage inductances (H)
L_m	magnetizing inductance (H)

The final set of equations is the motion equation. It represents the rotor mechanical speed (ω_m) in terms of (T_e) and (T_m).

$$\begin{cases} J\dfrac{d\omega_n}{dt} = T_e - T_m \\ T_e = \dfrac{3P}{2}Re\left(j\vec{\psi}_s\vec{\imath}_s^{\star}\right) = -\dfrac{3P}{2}Re(j\vec{\psi}_r\vec{\imath}_r^{\star}) \end{cases} \quad (12)$$

Where,

J	moment of inertia of the rotor ($kg.m^2$)
T_e	electromagnetic torque ($N.m$)
T_m	mechanical torque from the generator shaft ($N.m$)
ω_m	rotor mechanical speed, $\omega_m = \omega_r/p$ (rad/s)
P	number of pole pairs

The other dynamic model of the induction generator is the dq-axis model, which is composed of two equivalent circuits, one for each axis as shown in Figure 18.

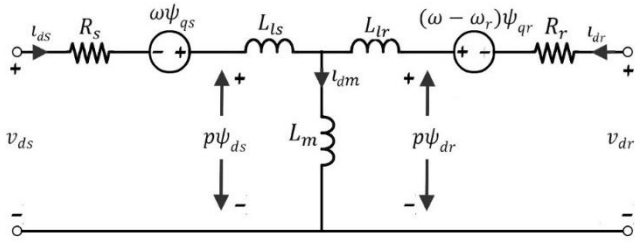

(a) d-axis equivalent circuit

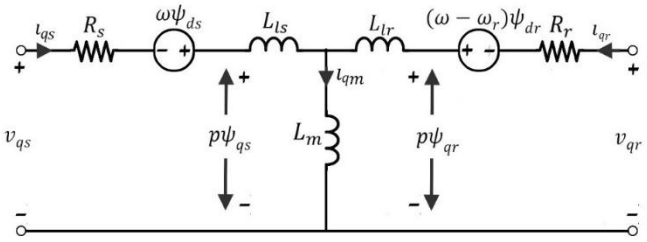

(b) q-axis equivalent circuit

Figure 18: dq-axis equivalent circuits of the IG.

The dq-axis model is derived from the space vector model and its equations are given by:

$$\begin{cases} \vec{v}_s = v_{ds} + jv_{qs} \\ \vec{i}_s = i_{ds} + ji_{qs} \\ \vec{\psi}_s = \psi_{ds} + j\psi_{qs} \\ \vec{v}_r = v_{dr} + jv_{qr} \\ \vec{i}_r = i_{dr} + ji_{qr} \\ \vec{\psi}_r = \psi_{dr} + j\psi_{qr} \end{cases} \tag{13}$$

By substituting equation (13) into equation (10) and rearrange it, the voltage equations of the dq-axis model can be derived:

$$\begin{cases} v_{ds} = R_s i_{ds} + p\psi_{ds} - \omega\psi_{qs} \\ v_{qs} = R_s i_{qs} + p\psi_{qs} + \omega\psi_{ds} \\ v_{dr} = R_r i_{dr} + p\psi_{dr} - (\omega - \omega_r)\psi_{qr} \\ v_{qr} = R_r i_{qr} + p\psi_{qr} + (\omega - \omega_r)\psi_{dr} \end{cases} \tag{14}$$

Similarly, the flux linkages of the dq-axis model can be obtained by substituting equation (13) into equation (11):

$$\begin{cases} \psi_{ds} = (L_{ls} + L_m)i_{ds} + L_m i_{dr} = L_s i_{ds} + L \\ \psi_{qs} = (L_{ls} + L_m)i_{qs} + L_m i_{qr} = L_s i_{qs} + L \\ \psi_{dr} = (L_{lr} + L_m)i_{dr} + L_m i_{ds} = L_r i_{dr} + I \\ \psi_{qr} = (L_{lr} + L_m)i_{qr} + L_m i_{qs} = L_r i_{qr} + L \end{cases} \tag{15}$$

Using the flux linkages and currents expressions of the dq-axis model, the electromagnetic torque T_e in equation (12) can be derived as:

$$T_e = \frac{3P}{2}\left(i_{qs}\psi_{ds} - i_{ds}\psi_{qs}\right) \tag{16}$$

For modelling the dq-axis model in MATLAB Simulink, the previous equations are rearranged to build the stages of the model, so equation (14) can be rewritten as:

$$\begin{cases} \psi_{ds} = (v_{ds} - R_s i_{ds} + \omega\psi_{qs})/s \\ \psi_{qs} = (v_{qs} - R_s i_{qs} - \omega\psi_{ds})/s \\ \psi_{dr} = (v_{dr} - R_r i_{dr} + (\omega - \omega_r)\psi_{qr})/s \\ \psi_{qr} = (v_{qr} - R_r i_{qr} - (\omega - \omega_r)\psi_{dr})/s \end{cases} \quad (17)$$

Where the Derivative Operator (p) is replaced by the Laplace Operator (s). Equation (15) can be represented in a matrix form:

$$\begin{bmatrix} \psi_{ds} \\ \psi_{qs} \\ \psi_{dr} \\ \psi_{qr} \end{bmatrix} = \begin{bmatrix} L_s & 0 & L_m & 0 \\ 0 & L_s & 0 & L_m \\ L_m & 0 & L_r & 0 \\ 0 & L_m & 0 & L_r \end{bmatrix} \begin{bmatrix} i_{ds} \\ i_{qs} \\ i_{dr} \\ i_{qr} \end{bmatrix} \quad (18)$$

From the previous equation, the currents can be expressed in terms of flux linkages by using the following matrix:

$$\begin{cases} [\psi] = [L][i] \\ [L]^{-1}[\psi] = [L]^{-1}[L][i] \\ [i] = [L]^{-1}[\psi] \end{cases} \quad (19)$$

From which

$$\begin{bmatrix} i_{ds} \\ i_{qs} \\ i_{dr} \\ i_{qr} \end{bmatrix} = \frac{1}{L_s L_r - L_m^2} \begin{bmatrix} L_r & 0 & -L_m & 0 \\ 0 & L_r & 0 & -L_m \\ -L_m & 0 & L_s & 0 \\ 0 & -L_m & 0 & L_s \end{bmatrix} \begin{bmatrix} \psi_{ds} \\ \psi_{qs} \\ \psi_{dr} \\ \psi_{qr} \end{bmatrix} \quad (20)$$

The final equations needed to build the model are the motion and the torque equations:

$$\begin{cases} \omega_r = \dfrac{P}{Js}(T_e - T_m) \\ T_e = \dfrac{3P}{2}(i_{qs}\psi_{ds} - i_{ds}\psi_{qs}) \end{cases} \quad (21)$$

Based on equations (17), (20), and (21), the model incorporates six input variables:

$v_{ds}, v_{qs}, v_{dr}, v_{qr}, \omega \text{ and } T_m$, and four output variables: $i_{ds}, i_{qs}, \omega_r \text{ and } T_e$. The block diagram used to simulate the induction generator is represented and shown in Figure 19.

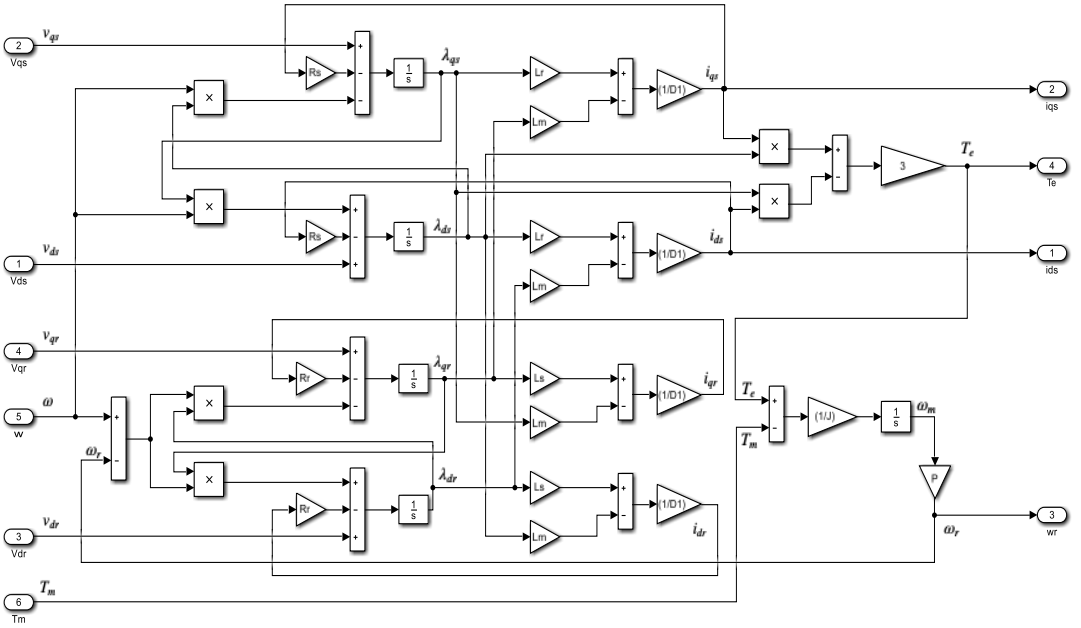

Figure 19: Block diagram of an induction generator.

To run the simulation model, the generator parameters are set according to Table 2.

Table 2: squirrel cage induction generator (SCIG) parameters

Symbol	Parameter	Value
L_m	Magnetizing Inductance	**2.13461 *mH***
J	Moment of Inertia	**1200 $kg.m^2$**
P	Number of Pole Pairs	**2**
V_{rated}	Rated Line-to-line Voltage	**690 *V*** (rms)
T_m	Rated Mechanical Torque	**14.74 *kN.M***
P_g	Rated output power	**2.3 *MW***
pf	Rated Power Factor	**0.888**
ω	Rated Rotor Speed	**1512 *rpm***
I_{rated}	Rated Stator Current	**2168 *A*** (rms)
f	Rated Stator Frequency	**50 *Hz***
L_r	Rotor Leakage Inductance	**0.06492 *mH***
R_r	Rotor Winding Resistance	**1.497 *m*Ω**
L_s	Stator Leakage Inductance	**0.06492** mH
R_s	Stator Winding Resistance	1.102 mΩ

By integrating the models of the wind turbine, the drive train, and the induction generator, a complete model of the wind power plant unit is obtained, which can be simulated to analyse

the output response based on the system's input variables. The block diagram of this system is presented in Figure 20.

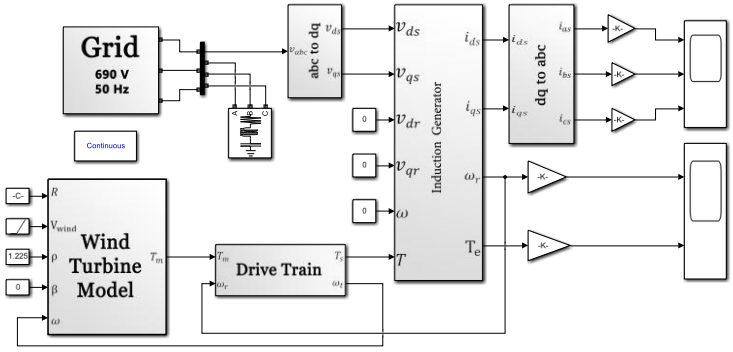

Figure 20: Block diagram for simulation of SCIG with direct grid connection.

The voltage and the frequency of the grid connected to the system are 690 v and 50 Hz respectively, and its curve is shown in Figure 21. The grid balanced voltages v_as, v_bs, and v_cs are transformed to the two-phase voltages v_ds, and v_qs through the abc/dq transformation.

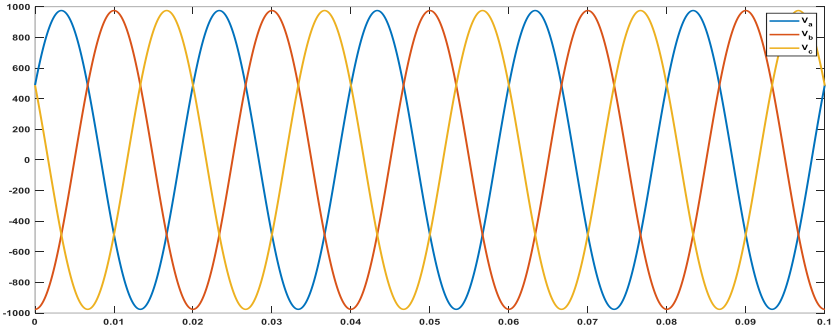

Figure 21: the voltage of the grid connected to the SCIG (690v,50Hz)

In case of squirrel-cage induction generators, rotor voltages v_dr, and v_qr are set to zero. To simulate the induction generator in the stationary reference frame, the speed of the arbitrary reference frame ω can be set to zero.

As mentioned in section 6.3, when there is no wind, the turbine will be in the parking mode and a circuit breaker is used to disconnect the generator terminals from the grid. When the wind rises and exceeds the cut-in speed, the blades will rotate and force the generator shaft to rotate as well. When, however, the generator is accelerated close to the rated speed, the circuit breaker is closed, and the generator is directly connected to the grid. By simulating the model shown in Figure 20, and during the system starts operating, excessive current flows into the generator as shown in Figure 22.

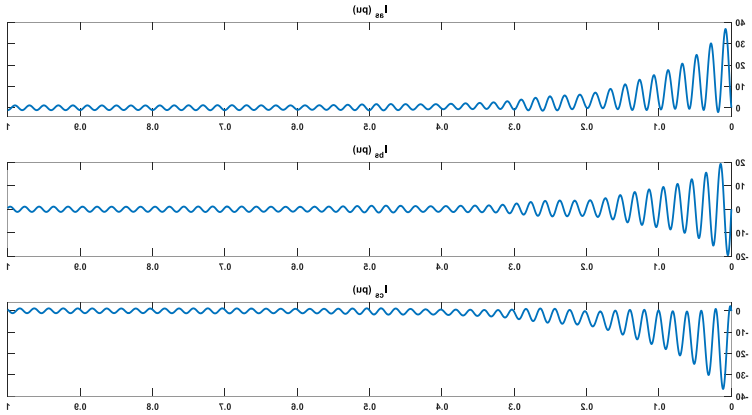

Figure 22: Current waveforms of SCIG with direct grid connection

When the current flows in the stator windings, a rotating magnetic field is established, producing an electromagnetic torque T_e. At the system start up, the generator operates below synchronous speed, functioning in motoring mode and, as a result, producing a positive torque that accelerates the turbine. As the generator speed increases and reaches synchronous speed, the system transitions to steady-state operation, as shown in Figure 23, enabling the turbine to capture wind power through the application of aerodynamic controls.

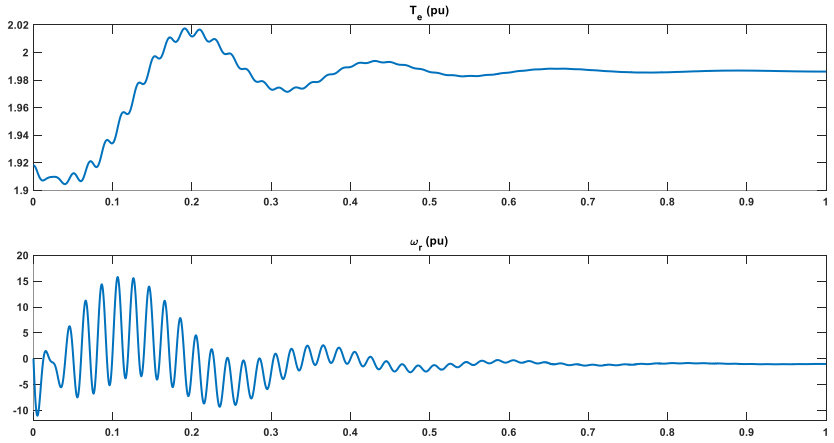

Figure 23: Torque and speed waveforms of SCIG with direct grid connection

9. Conclusion

The adoption of renewable energy sources has proven effective in reducing emissions and conserving fuel. Maximising the power output of wind turbines requires the attainment of the optimal performance coefficient, which is inherently linked to maintaining the tip speed ratio (TSR) at its ideal value under varying wind conditions. To achieve this, the turbine must be engineered to sustain a stable TSR, supported by optimising the angular speed of the rotor hub. The blade pitch angle is another important factor that influences power output, which

necessitate precise adjustments through aerodynamic control systems to respond to fluctuations in wind speed. Furthermore, the blade length must be carefully optimised during the design phase to ensure efficient energy capture while balancing structural and operational considerations. The drive train facilitates the integration of components with differing inertia constants, ensuring reliable energy transmission without the risk of damage.

The Squirrel Cage Induction Generator (SCIG) model, developed in MATLAB Simulink, shows the importance of addressing challenges such as torque oscillations and excessive inrush currents during system start-up, which preclude the direct grid connection of large SCIGs. These findings reinforce the necessity of technical precision and control strategies in the design and operation of wind energy systems, which, as a result, contribute to their broader integration into sustainable energy frameworks.

Acknowledgement

The authors acknowledge the guidance and support of Prof. Mahdi M. El-Arini, which have greatly contributed to the development of this work.

References

[1] M. M, J. P, and N. B. Kumar, "A Comparative Study of Maximum Power Tracking of Turbines of Wind Energy Conversion Systems," in 2022 International Conference on Futuristic Technologies in Control Systems & Renewable Energy (ICFCR), IEEE, Jul. 2022, pp. 1–6. doi: 10.1109/ICFCR54831.2022.9893580.

[2] A. Hesami and A. H. Nikseresht, "Performance Enhancements of Savonius Wind Turbine using a Hybrid Augmentation System," in 7th Iran Wind Energy Conference (IWEC2021), IEEE, May 2021, pp. 1–5. doi: 10.1109/IWEC52400.2021.9466964.

[3] Y. Song, M. Du, W. Zhao, and H. Lin, "A new integrated regulation strategy and modelling for wind turbine with battery energy storage system," J Energy Storage, vol. 63, p. 107111, Jul. 2023, doi: 10.1016/j.est.2023.107111.

[4] R. Bharani and A. Sivaprakasam, "A Review Analysis on Performance and Classification of Wind Turbine Gearbox Technologies," IETE J Res, vol. 68, no. 5, pp. 3341–3355, Sep. 2022, doi: 10.1080/03772063.2020.1756936.

[5] "NREA." Accessed: May 10, 2024. [Online]. Available: http://nrea.gov.eg/test/en/About/Intro

[6] "Wind Atlas." Accessed: May 10, 2024. [Online]. Available: http://nrea.gov.eg/test/en/Technology/WindAtlas

[7] https://www.power-technology.com/data-insights/power-plant-profile-zafarana-egypt/?cf-view.

[8] A. Chaudhuri, R. Datta, M. P. Kumar, J. P. Davim, and S. Pramanik, "Energy Conversion Strategies for Wind Energy System: Electrical, Mechanical and Material Aspects," Materials, vol. 15, no. 3, p. 1232, Feb. 2022, doi: 10.3390/ma15031232.

[9] M. Bourhis, M. Pereira, and F. Ravelet, "Experimental investigation of the effect of blade solidity on micro-scale and low tip-speed ratio wind turbines," Exp Therm Fluid Sci, vol. 140, p. 110745, Jan. 2023, doi: 10.1016/j.expthermflusci.2022.110745.

[10] S. Mehroliya, A. Arya, U. Mitra, P. Paliwal, and P. Mundra, "Comparative Analysis of Conventional Technologies and Emerging Trends in Wind Turbine Generator," in 2021 IEEE 2nd International Conference On Electrical Power and Energy Systems (ICEPES), IEEE, Dec. 2021, pp. 1–6. doi: 10.1109/ICEPES52894.2021.9699538.

[11] R. Quispe-Abad and N. Müller, "Finding an absolute maximum theoretical power coefficient for ducted wind turbines," Journal of Wind Engineering and Industrial Aerodynamics, vol. 236, p. 105335, May 2023, doi: 10.1016/j.jweia.2023.105335.

[12] H. Chen et al., "Improved torque compensation control based-maximum power point tracking strategy for large scale floating offshore wind turbines," Ocean Engineering, vol. 273, p. 113974, Apr. 2023, doi: 10.1016/j.oceaneng.2023.113974.

[13] C. A. Lopez-Villalobos, O. Martínez-Alvarado, O. Rodriguez-Hernandez, and R. Romero-Centeno, "Analysis of the influence of the wind speed profile on wind power production," Energy Reports, vol. 8, pp. 8079–8092, Nov. 2022, doi: 10.1016/j.egyr.2022.06.046.

[14] M. Yang, D. Wang, C. Xu, B. Dai, M. Ma, and X. Su, "Power transfer characteristics in fluctuation partition algorithm for wind speed and its application to wind power forecasting," Renew Energy, vol. 211, pp. 582–594, Jul. 2023, doi: 10.1016/j.renene.2023.05.004.

[15] J. Baruah, P. Venkaiah, N. Kumar, B. K. Sarkar, and N. Alom, "Offshore Wind Turbine Pitch Control with Aeroelastic Effect," in 2022 IEEE IAS Global Conference on Emerging Technologies (GlobConET), IEEE, May 2022, pp. 875–880. doi: 10.1109/GlobConET53749.2022.9872444.

[16] S. B. Abhi et al., "Design and Implementation of a Smart Wind Turbine with Yaw Mechanism," in 2023 3rd International Conference on Robotics, Electrical and Signal Processing Techniques (ICREST), IEEE, Jan. 2023, pp. 358–362. doi: 10.1109/ICREST57604.2023.10070075.

[17] S. Tang, D. Tian, X. Wu, M. Huang, and Y. Deng, "Wind turbine load reduction based on 2DoF robust individual pitch control," Renew Energy, vol. 183, pp. 28–40, Jan. 2022, doi: 10.1016/j.renene.2021.10.086.

[18] M. E. M. Salem, H. M. El-Batsh, A. A. El-Betar, and A. M. A. Attia, "Application of Neural Network Fitting for Pitch Angle Control of Small Wind Turbines," IFAC-PapersOnLine, vol. 54, no. 14, pp. 185–190, 2021, doi: 10.1016/j.ifacol.2021.10.350.

[19] D. Song et al., "Deep optimization of model predictive control performance for wind turbine yaw system based on intelligent fuzzy deduction," Expert Syst Appl, vol. 221, p. 119705, Jul. 2023, doi: 10.1016/j.eswa.2023.119705.

[20] D. Song, Q. Chang, S. Zheng, S. Yang, J. Yang, and Y. Hoon Joo, "Adaptive Model Predictive Control for Yaw System of Variable-speed Wind Turbines," Journal of Modern Power Systems and Clean Energy, vol. 9, no. 1, pp. 219–224, 2021, doi: 10.35833/MPCE.2019.000467.

[21] R. He, H. Yang, and L. Lu, "Optimal yaw strategy and fatigue analysis of wind turbines under the combined effects of wake and yaw control," Appl Energy, vol. 337, p. 120878, May 2023, doi: 10.1016/j.apenergy.2023.120878.

[22] Y. Li, X. Liang, A. Cai, L. Zhang, W. Lin, and M. Ge, "Effects of Blade Extension on Power Production and Ultimate Loads of Wind Turbines," Applied Sciences, vol. 13, no. 6, p. 3538, Mar. 2023, doi: 10.3390/app13063538.

[23] A. Chitransh, S. Kaur, and R. Parveen, "Comparative Analysis of Different Configuration of Generators for Extraction of Wind Energy," in 2021 Fifth International Conference on I-SMAC (IoT in Social, Mobile, Analytics and Cloud) (I-SMAC), IEEE, Nov. 2021, pp. 1765–1773. doi: 10.1109/I-SMAC52330.2021.9640627.